

UCLA

UCLA Previously Published Works

Title

Free-breathing diffusion tensor MRI of the whole left ventricle using second-order motion compensation and multitasking respiratory motion correction

Permalink

<https://escholarship.org/uc/item/41j9g2tg>

Journal

Magnetic Resonance in Medicine, 85(5)

ISSN

0740-3194

Authors

Nguyen, Christopher T
Christodoulou, Anthony G
Coll-Font, Jaume
[et al.](#)

Publication Date

2021-05-01

DOI

10.1002/mrm.28611

Peer reviewed



Published in final edited form as:

Magn Reson Med. 2021 May ; 85(5): 2634–2648. doi:10.1002/mrm.28611.

Free-breathing Diffusion Tensor MRI of the Whole Left Ventricle using Second Order Motion Compensation (M2) and Multitasking Respiratory Motion Correction (MT-MOCO)

Christopher T. Nguyen^{1,2,3,*}, Anthony G. Christodoulou^{4,5}, Jaume Coll-Font^{1,2,3}, Sen Ma^{4,5}, Yibin Xie⁴, Timothy G. Reese^{3,6}, Choukri Mekkaoui^{3,6}, Gregory D. Lewis^{2,7}, Xiaoming Bi⁸, David E. Sosnovik^{1,2,3,++}, Debiao Li^{4,5,++}

¹Cardiovascular Research Center, Massachusetts General Hospital, Charlestown, MA

²Department of Medicine, Harvard Medical School, Boston, MA

³A. A. Martinos Center for Biomedical Imaging, Massachusetts General Hospital, Charlestown, MA

⁴Biomedical Imaging Research Institute, Cedars-Sinai Medical Center, Los Angeles, CA

⁵Department of Bioengineering, University of California Los Angeles, Los Angeles, CA

⁶Department of Radiology, Harvard Medical School, Boston, MA

⁷Heart Failure Section, Cardiology Division, Massachusetts General Hospital, Boston, MA

⁸Siemens Medical Solutions USA, Inc., Los Angeles, CA

Abstract

Purpose—We aimed to develop a novel free-breathing cardiac diffusion tensor MRI (DT-MRI) approach, M2-MT-MOCO, capable of whole left ventricular coverage that leverages second order motion compensation (M2) diffusion encoding and Multitasking (MT) framework to efficiently correct for respiratory motion.

Methods—Imaging was performed in 16 healthy volunteers and 3 heart failure patients with symptomatic dyspnea. The healthy volunteers were scanned to compare the accuracy of interleaved multi-slice coverage of the entire left ventricle with a single-slice acquisition and the accuracy of the free-breathing conventional MOCO and MT-MOCO approaches with reference breath-hold (BH) DT-MRI. Mean diffusivity (MD), fractional anisotropy (FA), helix angle transmural (HAT) and intra-scan repeatability were quantified and compared.

Results—In all subjects, free-breathing M2-MT-MOCO DT-MRI yielded diffusion-weighted images of the entire left ventricle without bulk motion-induced signal loss. No significant differences were seen in the global values of MD, FA, and HAT in the multi-slice and single-slice acquisitions. Furthermore, global quantification of MD, FA, and HAT were also not significantly different between the MT-MOCO and BH, while conventional MOCO yielded significant

*Corresponding Author: Christopher Nguyen, PhD, Massachusetts General Hospital, Cardiovascular Research Center, 149 13th St, 4.213, Charlestown, MA 02138, Christopher.Nguyen@mgh.harvard.edu, 617-643-7838.

++ Contributed equally

differences in MD, FA, and HAT with MT-MOCO and FA with BH. In HF patients, M2-MT-MOCO DT-MRI was feasible yielding higher MD, lower FA, and lower HAT compared with healthy volunteers. Substantial agreement was found between repeated scans across all subjects for MT-MOCO.

Conclusion—M2-MT-MOCO enables free-breathing DT-MRI of the entire left ventricle in 10 minutes, while preserving quantification of myocardial microstructure compared to breath-held and single-slice acquisitions and is feasible in HF patients.

Keywords

Diffusion tensor MRI; cardiac magnetic resonance; motion correction; Multitasking; low rank tensor; myocardium; microstructure

INTRODUCTION

Diffusion tensor MRI (DT-MRI) is a powerful technique capable of resolving the architecture of cardiomyocytes in the heart (1–3) and characterizing the microstructural properties of the myocardium (4–6). The most widely used approach for cardiac DT-MRI involves a diffusion-encoded stimulated echo (STE) which has been used to detect changes in myocardial microstructure in ischemic injury and cardiomyopathy (7–12). However, if not ameliorated, STE DT-MRI is vulnerable to strain contamination (11,13). In addition, two adjacent heartbeats are required to generate a signal, limiting efficiency and complicating the use of conventional free-breathing techniques (14,15). Thus, multiple breath-holds are conventionally used which greatly reduces the potential for full anatomical coverage and places a significant burden on the patient.

Recent technical advances (16–18) have demonstrated that in vivo DT-MRI of the heart can be performed on clinical scanners using spin echo diffusion encoding and a second-order motion compensated gradient scheme (M2). A key advantage of the M2 spin echo over STE techniques is the ability to acquire diffusion encoded data in a single heartbeat. Consequentially, free-breathing acquisitions can be performed using conventional prospective navigator gating at every heartbeat (16). However, prospective navigator gating has limited efficiency (14,19), prolonging already lengthy scan times, and can result in the loss of steady state conditions. In contrast, retrospective respiratory motion correction (MOCO) can overcome these limitations and has been successfully implemented for late gadolinium enhanced (LGE) imaging and T1 mapping (20,21). These studies have shown that conventional MOCO in the short-axis plane is highly effective in correcting in-plane motion and shows a high degree of tolerance to low levels of through-plane motion.

We aimed here to implement a novel retrospective MOCO approach to mitigate respiratory motion in free-breathing cardiac DT-MRI and compare it with i) a standard breath-holding approach and ii) conventional MOCO algorithms. We present a modification to the motion correction paradigm, conceptually proposed in previous coronary MR angiography work (22–25), and tailor the approach specifically to in vivo M2 spin echo DT-MRI. Using a low-rank tensor approach, facilitated by Multitasking (26), we show that 100% of the acquired data can be utilized to efficiently separate respiratory motion from diffusion contrast over the

entire respiratory cycle. We hypothesized that the Multitasking MOCO (MT-MOCO) approach when combined with i) a modified spatially selective 2D RF excitation pulse and, ii) a multi-slice interleaved zoomed single shot EPI (z-EPI) readout (27), would allow free-breathing DT-MRI of the entire left ventricle (LV) to be performed in <15 minutes by acquiring a diffusion-weighted measurement at every heartbeat. To demonstrate the feasibility of this approach, DT-MRI was performed in a cohort of healthy human volunteers and in a small group of patients with heart failure and symptomatic dyspnea.

METHODS

Pulse Sequence Design

The 2DRF zoomed single shot echo planar imaging (z-EPI) (27) has several benefits conducive for cardiac imaging over conventional full FOV single shot EPI including a minimized temporal footprint (20 ms), improved spatial resolution, and reduced geometric distortion (Figure 1). The minimized temporal footprint also reduces blurring due to cardiac motion during the systolic acquisition. The 2DRF excitation pulse also has the added advantage of imaging subjects with high body-to-mass index since only a small FOV around the myocardium is excited. More importantly, 2DRF excitation facilitates a time-efficient interleaved multi-slice acquisition since only the reduced volume is excited in-plane. This is in contrast to conventional cross-pair inner volume excitation, which saturates the entire stack of slices for each single-slice acquisition. Diffusion encoding in the heart was achieved with B1-resistant second-order motion compensation (M2) spin echo (16), with max gradient amplitudes (80 mT/m) and half max gradient slew rates (100 mT/m/ms).

Through-plane motion, if severe enough, can cause cross-talk between slice excitations for multi-slice interleaved acquisitions resulting in significant errors in quantification. However, if a slice were to fully recover before it moves into its neighboring slice location, then cross-talk can be mitigated. Assuming normal myocardial T1, T2, and mean diffusivity at 3T (1280ms (28), 40ms (29), and $1.2 \mu\text{m}^2/\text{ms}$ (18) respectively), the T1 recovery over 4RR would account for ~90% signal recovery for a heart rate of 80 beats-per-minute ($\text{TR} \sim 2.34\text{T1}$), which would fully recover the signal loss incurred from T2 and diffusion decay (~90% loss). Consequentially, the proposed multi-slice interleaved reordering scheme acquired a single slice at each RR such that slices would recover over at least 4RR intervals before an adjacent slice was acquired again (e.g. $\text{slice}_{\text{index}} = (\text{slice}_{\text{index}-1} + N_{\text{TR}}) \% N_{\text{slices}} + \text{floor}((\text{index}) / N_{\text{TR}} - 1)$) for index = 1, 2, 3, ... etc. For $N_{\text{TR}} = 4$ and $N_{\text{slices}} = 12$, $\text{slice}_{\text{index}} = 1, 5, 9, 2, 6, 10, 3, 7, 11, 4, 8, 12$ and index = 1–12). This optimized scheme ensures that the adjacent slice is fully recovered, and the assumed mono-exponential diffusion signal model is valid. However, the optimized scheme does not address the potential impact of motion-induced blurring on the estimated self-diffusion tensor in the through-plane direction.

Retrospective Motion Correction for DT-MRI Parameter Mapping

Conventional Retrospective Respiratory Motion Correction (MOCO)—

Conventional retrospective respiratory motion correction (MOCO) has been performed for motion correction using a mutual information optimizer for T1 mapping (21), LGE (20), and T2 mapping (29). Conventional MOCO requires a target image which is typically the first

image in the acquired series for a given slice. To match respiratory phases on other slices, manual selection of targets for each slice is required, which for this study was the end expiratory phase.

MOCO was applied to the raw, uncorrected DT-MRI dataset by first cropping along the readout direction and then up-sampling to a final 256×256 matrix from the acquired 167×55 matrix. Cropping the image around the LV and up-sampling the matrix improves convergence of the co-registration by limiting the region of interest to the myocardium and increasing the number of input pixels. Each image for a given slice was then co-registered to the target image (end respiration) using open source software (Elastix (30)) that applies an affine transformation and then a non-rigid transformation optimized for mutual information. The process is repeated for all slices resulting in a total of $N_{\text{slices}} \times (N_{\text{DWI}} - 1) \times N_{\text{avg}} = 612$ co-registrations, where N_{slices} , N_{DWI} , and N_{AVG} are defined as number of slices, number of diffusion weighted images, and number of averages, respectively. Total computation time for the 612 registrations was 582 min for a single core Intel Xeon 3.0GHz CPU and 48min when parallelized across 12 cores.

Multitasking-based Retrospective Respiratory Motion Correction (MT-MOCO)

—Multitasking-based respiratory motion correction (MT-MOCO) minimizes the amount of co-registration needed by conventional MOCO (i.e. registering every image to a single reference) and overcomes the limitations introduced by contrast differences due to diffusion weighting which are inadequately addressed with multimodal image registration (e.g. mutual information). Instead, MT-MOCO uses low-rank tensor (LRT) modeling and a Multitasking framework (26) to cluster the acquired diffusion-weighted images into respiratory bins generating a diffusion-matched template image for each bin. LRT aims to recover the respiratory phases and model the acquired images with a low-rank tensor over the dimensions of space, diffusion encoding directions, and respiratory phases. Using the LRT framework, we can use k-means clustering to generate respiratory bin templates without being confounded by the image differences due to diffusion contrast. Then, the respiratory motion correction problem then reduces to determining the co-registration transforms of the respiratory bin templates for each slice (i.e. $N_{\text{slice}} \times N_{\text{bin}}$) as opposed to each individually acquired diffusion-weighted image (i.e. $N_{\text{slice}} \times N_{\text{DWI}} \times N_{\text{avg}}$). Another inherent advantage of MT-MOCO is that assuming every slice is imaged throughout the entire breathing cycle, all slices will automatically be co-registered to the same respiratory position without having to manually select the respiratory phase for each slice, which potentially allows for long axis reformatting and more coherent through-plane tractography.

The generalized framework behind MT-MOCO has been recently described (26) but can be briefly summarized in three major steps (Figure 2): 1) regress out the features related to diffusion contrast to obtain low rank images featuring only respiratory motion shifts, 2) bin the templates into respiratory bins and 3) co-register each respiratory bin to a reference respiratory bin. Before applying MT-MOCO, the $N_{\text{DWI}} \times N_{\text{avg}}$ acquired images, \mathcal{A} , are cropped and up-sampled following the same steps performed for conventional MOCO. The acquired images, \mathcal{A} , depict variable diffusion weighting, diffusion direction, and respiratory motion. To perform respiratory clustering, the impact of diffusion was regressed away from

the acquired images to produce low rank images \mathcal{A}_R featuring only respiratory motion shifts. This respiratory-only $(N_x \times N_y) \times N_{\text{DWI}} \times N_{\text{avg}}$ image tensor \mathcal{A}_R was estimated from the LRT decomposition of the identically-sized acquired image tensor \mathcal{A} using a high order singular value decomposition (HOSVD) (31). We express \mathcal{A} in the Tucker (32) form in Equation 1:

$$\mathcal{A} = \Phi_{\mathbf{t}} \times_1 \Phi_{\text{xy}}$$

$$\Phi_{\mathbf{t}} = \mathcal{G} \times_2 \Phi_{\text{DWI}} \times_3 \Phi_{\text{avg}} \quad (\text{Eq. 1})$$

where $\Phi_{\text{xy}}^{(N_x \times N_y) \times L_1}$ is the image basis matrix and $\Phi_{\mathbf{t}}^{L_1 \times N_{\text{DWI}} \times N_{\text{avg}}}$ is the temporal factor tensor, the latter of which comprises the Tucker core tensor $\mathcal{G}^{L_1 \times L_2 \times L_3}$, the diffusion basis matrix $\Phi_{\text{DWI}}^{N_{\text{DWI}} \times L_2}$, and the multiple-average basis matrix $\Phi_{\text{avg}}^{N_{\text{avg}} \times L_3}$. Note that L_j is the rank for a given basis matrix, and \times_m is the m^{th} mode tensor to matrix product, and \mathcal{A} is said to be rank- (L_1, L_2, L_3) (31). HOSVD was performed using the open-source Tensor Toolbox (www.tensortoolbox.org) in Matlab (Mathworks, Natick, MA) (33). By choosing a sufficient reduction in rank, L_1 (the dimensionality of the overall temporal factor $\Phi_{\mathbf{t}}$), higher-order temporal dynamics can be removed from \mathcal{A} . Because b-value dominates the difference between various images for in vivo DT-MRI, reconstructing \mathcal{A} with the lowest rank $L_1 = 1$, $\mathcal{A}^{L_1 = 1}$, primarily isolates b-value changes (Figure 2B, Supporting Information Video S1). With increasing rank L_1 , more temporal features of the original acquired images, \mathcal{A} , can be realized and compounded with the lower rank features. For example, for free-breathing cardiac DT-MRI, reconstruction of \mathcal{A} with $L_1 = 2$, $\mathcal{A}^{L_1 = 2}$, reveals inclusion of respiratory position shifts in addition to the b-value changes found in $\mathcal{A}^{L_1 = 2}$. \mathcal{A} reconstructed with $L_1 = 10$, $\mathcal{A}^{L_1 = 10}$, starts to reveal diffusion contrast predominantly influenced by diffusion gradient direction. Reconstruct of \mathcal{A} with full rank $L_1 = N_{\text{DWI}} \times N_{\text{avg}}$ will result in the original acquired image, \mathcal{A} . Because the truncated tensor $\mathcal{A}^{L_1 = 2}$, primarily depicts only b-value changes and respiratory shifts, it only requires b-value correction in order to be useful for respiratory binning. The b-value changes also dominate $\Phi_{\text{DWI}}^{L_2 = 1}$ (the first basis vector in Φ_{DWI}), so rescaling the truncated rank- $(2, L_2, L_3)$ tensor according to $\Phi_{\text{DWI}}^{L_2 = 1}$ results in images featuring only respiratory motion shifts, \mathcal{A}_R :

$$\mathcal{A}_R = \tilde{\Phi}_{\mathbf{t}} \times_1 \Phi_{\text{xy}}^{L_1 = 2}$$

$$\tilde{\Phi}_{\mathbf{t}} = \mathcal{G}^{L_1 = 2} \times_2 \left[\left(\Phi_{\text{DWI}}^{L_2 = 1} \right)^+ \Phi_{\text{DWI}} \right] \times_3 \Phi_{\text{avg}} \quad (\text{Eq. 2})$$

where realizing $\Phi_{\text{DWI}}^{L_2 = 1}$ is a vector, the b-value correction matrix is defined as

$$\left(\Phi_{\text{DWI}}^{L_2 = 1} \right)^+ = \left[\text{diag} \left(\Phi_{\text{DWI}}^{L_2 = 1} \right) \right]^{-1}.$$

Finally, \mathcal{A}_R images were clustered into N_{bin} respiratory bins ($N_{\text{bin}} = 6$) using a k-means clustering algorithm and reordered from end expiration to end inspiration respiratory phases along a fitted line through the cluster centroids. The k-means clustering was initialized with a random solution and 100 replicates were performed to avoid local minima. Finally, the \mathcal{A}_R images closest to the k-means cluster centroids were used as N_{bin} respiratory template images with one template for each respiratory bin. The N_{bin} template images were co-registered to the end expiratory template image using the same open source software (Elastix (30)) used for conventional MOCO. After calculation of the N_{bin} co-registration transforms, represented with the deformation fields \mathbf{T} , each of the original acquired images was motion-corrected by directly applying the known transformation from the appropriate bin to which that image was assigned for each slice (Total computation time for all slices = 62 min on a single core Intel Xeon 3.0GHz CPU and 5 min when parallelized across 12 cores). All the acquired images in this scheme are used without any a-priori rejection of data. Note that because Φ_{xy} is orthonormal when calculated from the HOSVD, and therefore does not impact Euclidean distance calculations, k-means clustering produces identical results whether clustering $\mathcal{A}_R = \tilde{\Phi}_t \times_1 \Phi_{xy}^{L_1=2}$ or whether directly clustering $\tilde{\Phi}_t$.

DT-MRI Parameter Quantification—Following respiratory motion correction, pixel-wise values of mean diffusivity (MD), fractional anisotropy (FA), and helix angle (HA) were calculated using custom software (16) in Matlab (Mathworks, Natick, MA). Tensor reconstruction was calculated using a modified weighted least squares fit (34), where the weights are derived from the inverse of the regularized norm of the transformation matrix calculated from MT-MOCO given by:

$$\mathbf{y} = \mathbf{X}\boldsymbol{\beta} + \boldsymbol{\varepsilon} \quad (\text{Eq. 3})$$

$$\hat{\boldsymbol{\beta}} = (\mathbf{X}^T \mathbf{W} \mathbf{X})^{-1} \mathbf{X}^T \mathbf{W} \mathbf{y} \quad (\text{Eq. 4})$$

$$\mathbf{y} = [\ln(S_1) \ln(S_2) \dots \ln(S_N)]^T$$

$$\boldsymbol{\beta} = [D_{xx} \ D_{yy} \ D_{zz} \ D_{xy} \ D_{xz} \ D_{yz} \ \ln(S_0)]^T$$

$$\boldsymbol{\varepsilon} = [\varepsilon_1 \ \varepsilon_2 \ \dots \ \varepsilon_N]^T$$

$$\mathbf{X} = -b \begin{bmatrix} G_{x1}^2 & G_{y1}^2 & G_{z1}^2 & 2G_{x1}G_{y1} & 2G_{x1}G_{z1} & 2G_{y1}G_{z1} & 1 \\ G_{x2}^2 & G_{y2}^2 & G_{z2}^2 & 2G_{x2}G_{y2} & 2G_{x2}G_{z2} & 2G_{y2}G_{z2} & 1 \\ \vdots & \vdots & \vdots & \vdots & \vdots & \vdots & \vdots \\ G_{xN}^2 & G_{yN}^2 & G_{zN}^2 & 2G_{xN}G_{yN} & 2G_{xN}G_{zN} & 2G_{yN}G_{zN} & 1 \end{bmatrix}$$

$$\mathbf{W} = \begin{bmatrix} \rho_1 & 0 & \dots & 0 \\ 0 & \rho_2 & 0 & \vdots \\ \vdots & 0 & \ddots & 0 \\ 0 & \dots & 0 & \rho_N \end{bmatrix}$$

$$\rho_i = \frac{1}{1 + \|\mathbf{T}_i\|_2^2}$$

where equation 4 solves the least squares representation of solving for the array (β) of the desired diffusion coefficients (D) in Equation 3. \mathbf{y} defines the vector of acquired diffusion-weighted signals (S_i) with noise (ϵ) for each pixel and DW image ($i \in [1, N]$), \mathbf{X} defines the design matrix of matching diffusion gradient encodings (G_i) weighted by b-value (b), and \mathbf{W} defines the weighting matrix of the regularized inverse norm. The latter is formed by the diagonal coefficients ρ_i , computed with the displacement vector \mathbf{T}_i , calculated from MT-MOCO for each voxel and DW image, i .

After calculating diffusion coefficients at each pixel, eigenvalue decomposition yielded eigenvectors to calculate cardiomyocyte orientation and eigenvalues to calculate MD and FA (35). HA was calculated using the same geometric definition as Streeter, et al (36), with the local tangent vector, \mathbf{u} , being defined from the center of mass of the LV blood pool to the voxel of interest for each short axis slice.

The left ventricle (LV) was manually segmented for the mean LV estimates of MD and FA. Mean LV HA transmural depth (HAT, or the slope of mean HA vs transmural depth) was measured in lieu of the mean LV HA. For each short axis slice, HAT was calculated by automatically segmenting the LV into five transmural concentric rings, following which the slope was extracted from the linear regression of the mean HA for each ring against the transmural depth.

In vivo Imaging

Scanning was performed on a 3T clinical MRI system (MAGNETOM Prisma, Siemens Healthineers, Erlangen, Germany), equipped with an 80mT/m gradient system and a standard 32-channel antero-posterior surface coil. Imaging was performed in 16 healthy volunteers (8 females, 25±15 years old, heart rate = 58±13 BPM) and 3 subjects with symptomatic dyspnea (2 females, 75±14 years old, heart rates = 81±15 BPM), recruited from the heart failure (HF) clinic at the MGH. All subjects provided written consent in

accordance with a research protocol approved by the institutional review board of the Massachusetts General Hospital. Localizers and bSSFP CINE imaging were performed before DT-MRI with the following parameters: TR/TE = 3.4/1.6ms, $\alpha = 50^\circ$, 35 cardiac phases, $1.4 \times 1.4 \times 6\text{mm}^3$). Additionally, single shot bSSFP images in the 4-chamber orientation were acquired under free-breathing conditions to assess the amount of through-plane respiratory motion. For all DT-MRI acquisitions, single shot M2 z-EPI was used with the following parameters: 1 b0, 12 directions at $b = 500 \text{ s/mm}^2$, diffusion preparation time = 61ms, $1.8 \times 1.8 \times 8\text{mm}^3$, 1/3 reduced FOV, 2DRF pulse duration = 18.87ms, FOV = 300mm, Matrix=167×55, echo spacing = 0.53ms, EPI readout duration = 22ms, Partial Fourier = 6/8, TE=72ms, 4 averages. To determine the accuracy of the multi-slice free-breathing approach, single-slice and breath-hold acquisitions were also performed. The number of slices (N_{slices}), TR, number of diffusion weighted images (N_{DWI}), and number of averages (N_{AVG}) in the acquisitions were varied as outlined below (Table 1). CINE imaging and a scout trigger DT-MRI acquisition were used to manually determine the optimal trigger delay during end systole.

In the cohort of healthy volunteers, four DT-MRI protocols were performed to test various aspects of the proposed technique in a 70-minute scan (Table 1):

- i. *Free-breathing whole LV interleaved multi-slice with 12RR TR (MS-12RR)*: The proposed technique employed an interleaved multi-slice acquisition with a single slice being acquired during each RR interval (Figure 1). Twelve short axis slices were acquired to cover the entire LV. Consequentially, TR was set to 12RR with a total predictable scan time of (number of slices) \times (number of diffusion-weighted images) \times (number of averages) = $N_{\text{slices}} \times N_{\text{DWI}} \times N_{\text{AVG}} = 624\text{RR}$.
- ii. *Free-breathing single-slice with 12RR TR (SS-12RR)*: To test the effect of the optimized interleaved multi-slice acquisition, a free-breathing single-slice acquisition was performed at the basal, mid, and apical positions in the LV, using the same parameters as the MS-12RR protocol above. Note each short axis slice was allowed to recover 12RR before the next short axis slice was acquired to match TR between the MS-12RR and SS-12RR protocols.
- iii. *Breath-held single-slice with 1RR TR with (SS-1RR-BH)*: To compare the impact of free-breathing, reference breath-hold scans at basal, mid, and apical slices were acquired over 8 breath-holds, with each breath-hold acquiring a 12 direction DT-MRI dataset and a b0 image. A TR of 1RR interval was used to keep the breath-hold under 20 seconds. The subject was allowed to recover from each breath-hold for 13RR.
- iv. *Free-breathing single-slice with 1RR TR (SS-1RR)*: Analogous to the SS-1RR-BH protocol but performed under free-breathing conditions with the same TR of 1RR.

In the healthy volunteers, the MS-12RR scan was performed a second time, at the end of the scan slot to assess the accuracy and repeatability of the approach. In addition, the cohort of patients with heart failure were imaged with the MS-12RR protocol twice in a single scan session, with the two acquisitions separated by at least 30 minutes. This allowed the

technical feasibility and repeatability of the MT-MOCO approach to be tested in subjects with erratic and irregular breath-hold patterns.

Image Analysis

LV Segmentation and Sharpness Comparisons—LV epicardial and endocardial borders were manually segmented in the conventional MOCO and MT-MOCO datasets to quantify the total LV area of mis-registration compared across all slices with reference to the b0 images. The reference b0 images were chosen for each slice from the end respiratory bin selected during MT-MOCO co-registration and were set as the target image for each slice. The final LV mask was split into 16 American Heart Association (AHA) segments for regional analysis.

LV sharpness of the mean image across all diffusion-weighted images (DWIs) was compared for conventional MOCO, MT-MOCO, and breath-hold reconstructions defined by the inverse of the distance of the 20–80% of the maximum signal intensity (37) at the lateral and septal walls of the LV along a line defined by the midpoint of each wall and the center of mass of the blood pool. The sharpness measurement used LV sharpness was calculated for all slices for SS-IRR and SS-IRR-BH protocols and averaged for a global value.

Through-plane Displacement Maps—Displacement maps were created to assess the impact of through-plane motion on the MT-MOCO DT-MRI approach. ECG triggered single shot SSFP images, acquired in the 4-chamber view of the LV during free-breathing, were used as input to reconstruct time-resolved voxelwise displacement maps in the slice-encoding direction using conventional feature tracking (38).

Statistics—Wilcoxon-signed rank statistics were performed to test for significant differences with significance defined as $p < 0.05$ unless otherwise specified above. To test for repeatability, Bland-Altman plots (39) and intra-class correlation (ICC) (40) were analyzed. For AHA segmental analysis, we performed a one-way Kruskal-Wallis to test for differences between segments. When multiple comparisons were made a Bonferroni correction was performed reducing the significance level of $p < 0.05$ to $p < 0.05 / (\text{number of comparisons})$. Results are reported in median and interquartile range (IQR = 75% quartile - 25% quartile) expressed as median [IQR].

RESULTS

In all subjects, the free-breathing M2 MT-MOCO technique yielded raw DWIs of the entire LV without bulk motion-induced signal loss (Figure 3 and Supporting Information Figure S1). DT-MRI parameter maps were relatively uniform across all slices with no major striping artifacts seen in the long axis view due to possible through-slice motion and no significant differences among AHA segments across all healthy volunteers for MD, FA, and HAT. The HA maps revealed a smooth transition in HA from endocardium to epicardium, which could be visualized in both short axis and long axis views.

The quality of the MS-12RR images was equivalent to the images acquired with the SS-12RR approach under free-breathing acquisition. A comparison of the MS-12RR and SS-12RR protocols is shown in Figure 4. No regional differences were observed between the two protocols in the basal, mid, and apical slices. In addition, no significant differences were seen in the global values of MD (MS-12RR: 1.28 [0.18] $\mu\text{m}^2/\text{ms}$; SS-12RR: 1.21 [0.15] $\mu\text{m}^2/\text{ms}$, $p = \text{ns}$), FA (MS-12RR: 0.29 [0.06]; SS-12RR: 0.29 [0.06], $p = \text{ns}$), and HAT (MS-12RR: 1.11 [0.12] $^\circ/\%$; SS-12RR: 1.12 [0.15] $^\circ/\%$, $p = \text{ns}$) in the multi-slice and single-slice approaches. Further analysis revealed significant correlation (ICC = 0.82, 0.89 and 0.86, respectively) and minimal bias (bias % = 0.36%, 0.55%, and -0.24%) for the global MD, FA and HAT values. Bland-Altman plots also showed no apparent errors in the data distribution ruling out type 1 (proportional error trend) and 2 (inconsistent variability) errors {Riffenburgh:2012vz}. A regional analysis of MD, FA and HAT values at the base, mid-LV and apex also showed no significant differences and strong agreement (Table 2). Average scan times for MS-12RR and SS-12RR were 10.2 [1] min and 32.4 [3] min respectively with average heart-rate of 64 [8] BPM.

Comparison of the SS-1RR-BH and SS-1RR protocols yielded no significant increase in LV mis-registration area and no significant difference in sharpness between the MT-MOCO (epicardium misregistration area: 100 [18] mm^2 ; sharpness: 0.40 [0.09] mm^{-1} ; endocardial misregistration area: 93 [15] mm^2 ; sharpness: 0.43 [0.07] mm^{-1}) and breath-hold reconstructions (epicardium misregistration area: 92 [14] mm^2 ; sharpness: 0.45 [0.09] mm^{-1} ; endocardial misregistration area: 80 [11] mm^2 ; sharpness: 0.45 [0.09] mm^{-1}) (Figure 5). For conventional MOCO, a significant (46%; $p < 0.025$) increase in LV mis-registration area and decrease (31%; $p < 0.025$) in sharpness were found (epicardium misregistration area: 135 [29] mm^2 ; sharpness: 0.28 \pm 0.06 mm^{-1} ; endocardial misregistration area: 115 [14] mm^2 ; sharpness: 0.33 [0.12] mm^{-1}) compared to breath-hold reconstructions. MT-MOCO exhibited significantly ($p < 0.05$) less LV mis-registration area and improved sharpness when compared to conventional MOCO. Both conventional MOCO and MT-MOCO yielded significant ($p < 0.05$) decrease in LV mis-registration area and increase in sharpness when compared to naïve free-breathing reconstruction (epicardium misregistration area: 272 [31] mm^2 ; sharpness: 0.14 [0.04] mm^{-1} ; endocardial misregistration area: 234 [16] mm^2 ; sharpness: 0.14 [0.02] mm^{-1}).

Global quantification of MD (SS-1RR-BH: 1.23 [0.18] $\mu\text{m}^2/\text{ms}$; SS-1RR-MT-MOCO: 1.26 [0.14] $\mu\text{m}^2/\text{ms}$, $p = \text{ns}$), FA (SS-1RR-BH: 0.31 [0.05]; SS-1RR-MT-MOCO: 0.30 [0.06], $p = \text{ns}$), and HAT (SS-1RR-BH: 1.11 [0.14] $^\circ/\%$; SS-1RR-MT-MOCO: 1.10 [11] $^\circ/\%$, $p = \text{ns}$), revealed significant agreement (ICC = 0.78, 0.91, and 0.78, respectively) and minimal bias (bias % = 2.17%, 2.45%, -0.39% , respectively) between the MT-MOCO and breath-hold reconstructions (Figure 6 and Supporting Information Figure S2). Bland-Altman plots also showed no apparent errors in the global parameter values, ruling out type I and II errors, and no regional differences between the breath-hold and MT-MOCO reconstruction (Table 2). However, as shown in Table 2, conventional MOCO resulted in significant differences in global FA (SS-1RR-MOCO: 0.39 [0.15]; $p < 0.025$) compared with breath-hold reconstruction while MD (SS-1RR-MOCO: 1.33 [0.27] $\mu\text{m}^2/\text{ms}$, $p = 0.04$) and HAT (SS-1RR-MOCO: 0.95 [0.25] $^\circ/\%$, $p = 0.04$) were not significantly different despite a moderate bias (19.4% and -13.3% , respectively). The correlation between MT-MOCO and

the gold-standard SS-1RR-BH acquisition was also significant ($p < 0.025$) for MD, FA, and HAT, while the correlation between conventional MOCO and SS-1RR-BH was not significant for MD ($p = 0.04$), FA ($p = 0.03$), and HAT ($p = 0.67$). In addition, computation time for MT-MOCO (total = 5.2 [0.14] min, LRT = 59.3 [1.5] sec, k-means clustering = 11 [0.65] sec) was 9.4x less than conventional MOCO (48.5 [6] min) across all subjects.

The potential impact of through-plane motion on MT-MOCO is shown in Figure 7, where through-plane motion has been measured by feature tracking. The apical slices exhibited the most through-slice motion (2.7 [6.9] mm) compared with the base (1.5 [3.9] mm) and mid (0.84 [4.2] mm) slices (Figure 7). Long axis reconstruction of the 2D data did not reveal any significant striping or slice mismatch due to through-slice motion. In addition, no significant differences were found for MD, FA, and HA across all slices except the most apical slice between free-breathing MT-MOCO and breath-holding acquisitions (bias = 0.153 $\mu\text{m}^2/\text{ms}$, 0.212, and -0.126 deg/%; all $p < 0.05$).

The MS-12RR whole LV protocol was successfully completed in all subjects with heart failure, demonstrating the feasibility of the approach in subjects with irregular and erratic respiratory patterns (Figure 8 and Supporting Information Figure S3). The repeatability of M2 MT-MOCO (MS-12RR protocol) between the first and repeat scans was high. No significant differences were seen across all subjects in any of the measured parameters: MD (scan 1: 1.22 [0.14] $\mu\text{m}^2/\text{ms}$; scan 2: 1.23 [0.16] $\mu\text{m}^2/\text{ms}$, $p = \text{ns}$), FA (scan 1: 0.27 [0.06]; scan 2: 0.27 [0.06], $p = \text{ns}$), and HAT (scan 1: 1.15 [0.11] %; scan 2: 1.12 [0.14] %, $p = \text{ns}$). Correlation analysis showed substantial agreement between the two scans (ICC = 0.85, 0.93, and 0.92 respectively) and minimal bias (bias % = -0.90% , 0.21% , and -0.44% , respectively). Trends towards higher MD (MD scan 1: 16.1%; scan 2: 18.3%, $p = \text{ns}$), lower FA (FA scan 1: -30.1% ; scan 2: -32.8% , $p = \text{ns}$), and reduced HAT (HAT scan 1: -23.7% ; scan 2: -22.0% , $p = \text{ns}$) were seen in the heart failure cohort compared to healthy volunteers, which was powered primarily to demonstrate the feasibility of the technique. Importantly, the repeatability of the data in the subjects with heart failure was also high with substantial agreement in MD, FA and HAT values (ICC = 0.72, 0.82, 0.72, respectively) and minimal bias (bias % = 1.51%, 1.12%, and -0.68% respectively) between the two scans.

DISCUSSION

We present a novel free-breathing cardiac DT-MRI technique (M2-MT-MOCO) capable of whole LV acquisition in less than 15 minutes. The approach was based on the use of an optimized multi-slice interleaved single shot 2D RF z-EPI readout, second-order motion compensated (M2) diffusion encoding, and retrospective MT-MOCO. MT-MOCO was introduced as a novel approach to efficiently correct in-plane respiratory shifts and the calculated co-registration transforms can also be used as priors for the reconstruction of the self-diffusion tensor. The combination of these technologies facilitated 100% data utilization and predictable scan times dependent on a fixed number of RR intervals. Furthermore, MT-MOCO reduced computation time compared with conventional MOCO by over 9-fold across all subjects due MT-MOCO only determining motion registration transforms for each bin following an expected reduction of approximately $N_{\text{avg}} \times N_{\text{DWI}} / N_{\text{bins}}$. Most importantly, we demonstrate that M2 MT-MOCO can preserve DT-MRI parameter

quantification, including MD, FA, and HA, under free-breathing conditions more accurately than conventional MOCO and with similar accuracy to breath-hold DT-MRI.

One of the limitations of the M2-MT-MOCO DT-MRI technique is that it only corrects for in-plane motion and, consequentially, the degree of through-plane motion must be sufficiently low. However, with the technique used in this study, respiratory motion would not result in bulk motion-induced signal corruption of the diffusion contrast due to M2 spin echo diffusion encoding, but instead would result in pixelwise shifts and mismatch if uncorrected. MT-MOCO is well poised to correct in-plane pixelwise misregistration due to in-plane shifts being detected and characterized with an LRT model in the acquired 2D image. However, through-plane motion cannot be corrected due to the lack of through-plane encoding (i.e. 3D vs 2D phase encoding). Thus, an optimized slice interleaving scheme was implemented to allow for neighboring slices to be acquired after at least 4RR recovery, which would at least mitigate crosstalk due to incomplete T1 recovery. Previous free-breathing DT-MRI acquisition using prospective slice following to correct for through-slice motion has already been investigated (5). While head-to-foot motion during respiration was found to be on the order of the acquired slice thickness (8–10mm), through-plane motion in this study along the long axis of the heart was notably less (base: 0.84 [4.2] mm; mid: 1.5 [3.9] mm; apex 2.7 [6.9] mm) across all subjects (Figure 7). Consequently, long axis reconstruction of the 2D data did not reveal significant striping or other artifacts due to slice mismatch and/or crosstalk related to through-plane motion. These results are consistent with previous findings (20,21), in which through-plane motion was found to be minimal in the short axis orientation compared with long axis orientation for slices with 6–10mm thickness. Furthermore, no significant differences in MD, FA, and HA were seen between free-breathing MT-MOCO and breath-holding acquisitions except at the most apical slice location. Future improvements to the proposed sequence could easily integrate prospective slice-following, which would likely minimize any residual errors in the apical slice and allow for thinner slice thicknesses.

Another limitation of the M2-MT-MOCO DT-MRI paradigm involves the assumption that the dominating features of the acquired images are generated solely from diffusion-weighted contrast and thus can be regressed away to reveal respiratory motion shifts. We show that this assumption is valid both in healthy volunteers and a small cohort of subjects with heart failure and more complex respiratory patterns. While the aim of this study was to demonstrate the technical feasibility of the M2-MT-MOCO approach in patients with heart failure, the trends seen in the metrics of diffusion in these subjects were in agreement with previous observations (41) {Riffenburgh:2012vz}(7,42)(7,41). In addition, these differences were highly repeatable between scans underscoring the feasibility of the approach.

Of note, moments of motion that are not nulled by the M2 diffusion-encoding pulse will produce motion-related signal dephasing that will be indistinguishable to the MT-MOCO algorithm from diffusion contrast. This limits the application of the technique to phases of the cardiac cycle where higher order (> 3) motion coefficients are negligible. This has been shown to be the case for M2 diffusion encoding at end systole for single heart beat encoding (16–18,43)(16–18,42), and is reproduced here for multi-slice encoding. Applying MT-MOCO to other key DT-MRI techniques, such as STEAM-based methods (11,14,44)

(11,14,43), may not easily be achieved since free-breathing may result in severe bulk-motion loss. Consequently, MT-MOCO would need to be extended to include another dimension to account for bulk motion-induced signal decay, which could be explored in future studies.

CONCLUSION

We present a novel computationally efficient technique, M2-MT-MOCO, that allows free-breathing multi-slice DT-MRI of the entire LV to be performed in 10 minutes and faithfully preserves quantification of myocardial microstructure compared to single-slice and breath-hold M2 DT-MRI. While further validation in clinical settings will be required, the technique addresses the current need for multiple breath-holds in DT-MRI of the heart and has high clinical translational potential.

Supplementary Material

Refer to Web version on PubMed Central for supplementary material.

Acknowledgements

We acknowledge the dedicated work of the Martinos Center for Biomedical Imaging and Cardiovascular Research Center staff in supporting the logistical operations underpinning the presented study. Supported in part by the following grants from the National Institutes of Health: R21EB024701 (CN), R01HL151704 (CN), R01HL135242 (CN), R01HL131635 (CM), R01HL141563 (DES) and R01EB028146 (DL, AGC)

REFERENCES

1. Mekkaoui C, Reese TG, Jackowski MP, Bhat H, Sosnovik DE. Diffusion MRI in the heart Vermathen P, editor. *NMR Biomed.* 2017;30:e3426. doi: 10.1002/nbm.3426.
2. Froeling M, Strijkers GJ, Nederveen AJ, Chamuleau SA, Luijten PR. Diffusion Tensor MRI of the Heart – In Vivo Imaging of Myocardial Fiber Architecture. *Curr Cardiovasc Imaging Rep* 2014;7:9276. doi: 10.1007/s12410-014-9276-y.
3. Reese TG, Weisskoff RM, Smith RN, Rosen BR, Dinsmore RE, Wedeen VJ. Imaging myocardial fiber architecture in vivo with magnetic resonance. *Magn. Reson. Med* 1995;34:786–791. doi: 10.1002/mrm.1910340603. [PubMed: 8598805]
4. Callot V, Bennett E, Decking UKM, Balaban RS, Wen H. In vivo study of microcirculation in canine myocardium using the IVIM method. *Magn. Reson. Med* 2003;50:531–540. doi: 10.1002/mrm.10568. [PubMed: 12939761]
5. Moulin K, Croisille P, Feiweier T, Delattre BMA, Wei H, Robert B, Beuf O, Viallon M. In vivo free-breathing DTI and IVIM of the whole human heart using a real-time slice-followed SE-EPI navigator-based sequence: A reproducibility study in healthy volunteers. *Magn. Reson. Med* 2015;76:70–82. doi: 10.1002/mrm.25852. [PubMed: 26301785]
6. Spinner GR, Deuster von C, Tezcan KC, Stoeck CT, Kozerke S. Bayesian intravoxel incoherent motion parameter mapping in the human heart. *Journal of Cardiovascular Magnetic Resonance* 2017;19:85. doi: 10.1186/s12968-017-0391-1. [PubMed: 29110717]
7. Nielles-Vallespin S, Khalique Z, Ferreira PF, et al. Assessment of Myocardial Microstructural Dynamics by In Vivo Diffusion Tensor Cardiac Magnetic Resonance. *Journal of the American College of Cardiology* 2017;69:661–676. doi: 10.1016/j.jacc.2016.11.051. [PubMed: 28183509]
8. Ferreira PF, Kilner PJ, McGill L-A, et al. In vivo cardiovascular magnetic resonance diffusion tensor imaging shows evidence of abnormal myocardial laminar orientations and mobility in hypertrophic cardiomyopathy. *Journal of Cardiovascular Magnetic Resonance* 2014;16:445. doi: 10.1186/s12968-014-0087-8.

9. Mekkaoui C, Jackowski MP, Kostis WJ, Stoeck CT, Thiagalingam A, Reese TG, Reddy VY, Ruskin JN, Kozerke S, Sosnovik DE. Myocardial Scar Delineation Using Diffusion Tensor Magnetic Resonance Tractography. *J Am Heart Assoc* 2018;7. doi: 10.1161/JAHA.117.007834.
10. Wu M-T, Tseng W-YI, Su M-YM, Liu C-P, Chiou K-R, Wedeen VJ, Reese TG, Yang C-F. Diffusion tensor magnetic resonance imaging mapping the fiber architecture remodeling in human myocardium after infarction: correlation with viability and wall motion. *Circulation* 2006;114:1036–1045. doi: 10.1161/CIRCULATIONAHA.105.545863. [PubMed: 16940196]
11. Stoeck CT, Kalinowska A, Deuster von C, et al. Dual-phase cardiac diffusion tensor imaging with strain correction. Leemans A, editor. *PLoS ONE* [Internet] 2014;9:e107159. doi: 10.1371/journal.pone.0107159.
12. Sosnovik DE, Wang R, Dai G, Reese TG, Wedeen VJ. Diffusion MR tractography of the heart. *Journal of Cardiovascular Magnetic Resonance* 2009;11:47. doi: 10.1186/1532-429X-11-47. [PubMed: 19912654]
13. Tseng WY, Reese TG, Weisskoff RM, Wedeen VJ. Cardiac diffusion tensor MRI in vivo without strain correction. *Magn. Reson. Med* 1999;42:393–403. doi: 10.1002/(sici)1522-2594(199908)42:2<393::aid-mrm22>3.0.co;2-f. [PubMed: 10440965]
14. Nielles-Vallespin S, Mekkaoui C, Gatehouse P, et al. In vivo diffusion tensor MRI of the human heart: Reproducibility of breath-hold and navigator-based approaches. *Magn. Reson. Med* 2012;70:454–465. doi: 10.1002/mrm.24488. [PubMed: 23001828]
15. Mekkaoui C, Reese TG, Jackowski MP, Cauley SF, Setsompop K, Bhat H, Sosnovik DE. Diffusion Tractography of the Entire Left Ventricle by Using Free-breathing Accelerated Simultaneous Multisection Imaging. *Radiology* 2017;282:850–856. doi: 10.1148/radiol.2016152613. [PubMed: 27681278]
16. Nguyen C, Fan Z, Xie Y, Pang J, Speier P, Bi X, Kobashigawa J, Li D. In vivo diffusion-tensor MRI of the human heart on a 3 tesla clinical scanner: An optimized second order (M2) motion compensated diffusion-preparation approach. *Magn. Reson. Med* 2016;76:1354–1363. doi: 10.1002/mrm.26380. [PubMed: 27550078]
17. Aliotta E, Wu HH, Ennis DB. Convex optimized diffusion encoding (CODE) gradient waveforms for minimum echo time and bulk motion-compensated diffusion-weighted MRI. *Magn. Reson. Med* 2017;77:717–729. doi: 10.1002/mrm.26166. [PubMed: 26900872]
18. Stoeck CT, Deuster von C, Genet M, Atkinson D, Kozerke S. Second-order motion-compensated spin echo diffusion tensor imaging of the human heart. *Magn. Reson. Med* 2016;75:1669–1676. doi: 10.1002/mrm.25784. [PubMed: 26033456]
19. Bosak E Navigator motion correction of diffusion weighted 3D SSFP imaging. *Magnetic Resonance Materials in Biology, Physics, and Medicine* 2001;12:167–176. doi: 10.1016/S1352-8661(01)00113-2.
20. Kellman P, Larson AC, Hsu L-Y, Chung Y-C, Simonetti OP, McVeigh ER, Arai AE. Motion-corrected free-breathing delayed enhancement imaging of myocardial infarction. *Magn. Reson. Med* 2005;53:194–200. doi: 10.1002/mrm.20333. [PubMed: 15690519]
21. Xue H, Shah S, Greiser A, Guetter C, Littmann A, Jolly M-P, Arai AE, Zuehlsdorff S, Guehring J, Kellman P. Motion correction for myocardial T1 mapping using image registration with synthetic image estimation. *Magn. Reson. Med* 2011;67:1644–1655. doi: 10.1002/mrm.23153. [PubMed: 22135227]
22. Pang J, Sharif B, Arsanjani R, Bi X, Fan Z, Yang Q, Li K, Berman DS, Li D. Accelerated whole-heart coronary MRA using motion-corrected sensitivity encoding with three-dimensional projection reconstruction. *Magn. Reson. Med* 2014;73:284–291. doi: 10.1002/mrm.25097. [PubMed: 24435956]
23. Pang J, Bhat H, Sharif B, Fan Z, Thomson LEJ, LaBounty T, Friedman JD, Min J, Berman DS, Li D. Whole-heart coronary MRA with 100% respiratory gating efficiency: Self-navigated three-dimensional retrospective image-based motion correction (TRIM). *Magn. Reson. Med* 2013;71:67–74. doi: 10.1002/mrm.24628. [PubMed: 23401157]
24. Pang J, Sharif B, Fan Z, Bi X, Arsanjani R, Berman DS, Li D. ECG and navigator-free four-dimensional whole-heart coronary MRA for simultaneous visualization of cardiac anatomy and function. *Magn. Reson. Med* 2014;72:1208–1217. doi: 10.1002/mrm.25450. [PubMed: 25216287]

25. Bhat H, Ge L, Nielles-Vallespin S, Zuehlsdorff S, Li D. 3D radial sampling and 3D affine transform-based respiratory motion correction technique for free-breathing whole-heart coronary MRA with 100% imaging efficiency. *Magn. Reson. Med* 2011;65:1269–1277. doi: 10.1002/mrm.22717. [PubMed: 21500255]
26. Christodoulou AG, Shaw JL, Nguyen C, Yang Q, Xie Y, Wang N, Li D. Magnetic resonance multitasking for motion-resolved quantitative cardiovascular imaging. *Nature Biomedical Engineering* 2018 2:4 2018;2:215–226. doi: 10.1038/s41551-018-0217-y.
27. Riffel P, Michaely HJ, Morelli JN, Pfeuffer J, Attenberger UI, Schoenberg SO, Haneder S. Zoomed EPI-DWI of the pancreas using two-dimensional spatially-selective radiofrequency excitation pulses Reddy H, editor. *PLoS ONE* 2014;9:e89468. doi: 10.1371/journal.pone.0089468. [PubMed: 24594702]
28. Puntmann VO, Voigt T, Chen Z, et al. Native T1 Mapping in Differentiation of Normal Myocardium From Diffuse Disease in Hypertrophic and Dilated Cardiomyopathy. *JACC: Cardiovascular Imaging* 2013;6:475–484. doi: 10.1016/j.jcmg.2012.08.019. [PubMed: 23498674]
29. Yang H-J, Sharif B, Pang J, Kali A, Bi X, Cokic I, Li D, Dharmakumar R. Free-breathing, motion-corrected, highly efficient whole heart T2 mapping at 3T with hybrid radial-cartesian trajectory. *Magn. Reson. Med* 2015;75:126–136. doi: 10.1002/mrm.25576. [PubMed: 25753385]
30. Klein S, Staring M, Murphy K, Viergever MA, Pluim JPW. elastix: a toolbox for intensity-based medical image registration. *IEEE Trans. Med. Imaging* 2010;29:196–205. doi: 10.1109/TMI.2009.2035616.
31. Kolda TG, Bader BW. Tensor Decompositions and Applications. *SIAM Review* 2009;51:455–500. doi: 10.1137/07070111X.
32. Tucker LR. Some mathematical notes on three-mode factor analysis. *Psychometrika* 1966;31:279–311. doi: 10.1007/bf02289464. [PubMed: 5221127]
33. Bader BW, Kolda TG. Efficient MATLAB Computations with Sparse and Factored Tensors. *SIAM Journal on Scientific Computing* 2007;30:205–231. doi: 10.1137/060676489.
34. Chung S, Lu Y, Henry RG. Comparison of bootstrap approaches for estimation of uncertainties of DTI parameters. *NeuroImage* 2006;33:531–541. doi: 10.1016/j.neuroimage.2006.07.001. [PubMed: 16938472]
35. Basser PJ, Pierpaoli C. Microstructural and physiological features of tissues elucidated by quantitative-diffusion-tensor MRI. 1996. *J. Magn. Reson* 2011;213:560–570. doi: 10.1016/j.jmr.2011.09.022. [PubMed: 22152371]
36. Streeter DD, Spotnitz HM, Patel DP, Ross J, Sonnenblick EH. Fiber orientation in the canine left ventricle during diastole and systole. *Circulation Research* 1969;24:339–347. doi: 10.1161/01.RES.24.3.339. [PubMed: 5766515]
37. Li D, Carr JC, Shea SM, Zheng J, Deshpande VS, Wielopolski PA, Finn JP. Coronary Arteries: Magnetization-prepared Contrast-enhanced Three-dimensional Volume-targeted Breath-hold MR Angiography1. *Radiology* 2001;219:270–277. doi: 10.1148/radiology.219.1.r01ap37270. [PubMed: 11274569]
38. Schuster A, Stahnke V-C, Unterberg-Buchwald C, et al. Cardiovascular magnetic resonance feature-tracking assessment of myocardial mechanics: Intervendor agreement and considerations regarding reproducibility. *Clinical Radiology* 2015;70:989–998. doi: 10.1016/j.crad.2015.05.006. [PubMed: 26139384]
39. Bland JM, Altman DG. Statistical Methods for Assessing Agreement Between Two Methods of Clinical Measurement. *The Lancet* 1986;327:307–310. doi: 10.1016/S0140-6736(86)90837-8.
40. Rousson V, Gasser T, Seifert B. Assessing intrarater, interrater and test-retest reliability of continuous measurements. *Stat Med* 2002;21:3431–3446. doi: 10.1002/sim.1253. [PubMed: 12407682]
41. Riffenburgh R *Statistics in Medicine*. 3rd ed Academic Press; 2012.
42. Deuster von C, Sammut E, Asner L, Nordsletten D, Lamata P, Stoeck CT, Kozerke S, Razavi R. Studying Dynamic Myofiber Aggregate Reorientation in Dilated Cardiomyopathy Using In Vivo Magnetic Resonance Diffusion Tensor Imaging. *Circulation: Cardiovascular Imaging* 2016;9:H2308. doi: 10.1161/CIRCIMAGING.116.005018.

43. Nguyen C, Fan Z, Sharif B, He Y, Dharmakumar R, Berman DS, Li D. In vivo three-dimensional high resolution cardiac diffusion-weighted MRI: a motion compensated diffusion-prepared balanced steady-state free precession approach. *Magn. Reson. Med* 2014;72:1257–1267. doi: 10.1002/mrm.25038. [PubMed: 24259113]
44. Dou J, Reese TG, Tseng W-YI, Wedeen VJ. Cardiac diffusion MRI without motion effects. *Magn. Reson. Med* 2002;48:105–114. doi: 10.1002/mrm.10188. [PubMed: 12111937]

Author Manuscript

Author Manuscript

Author Manuscript

Author Manuscript

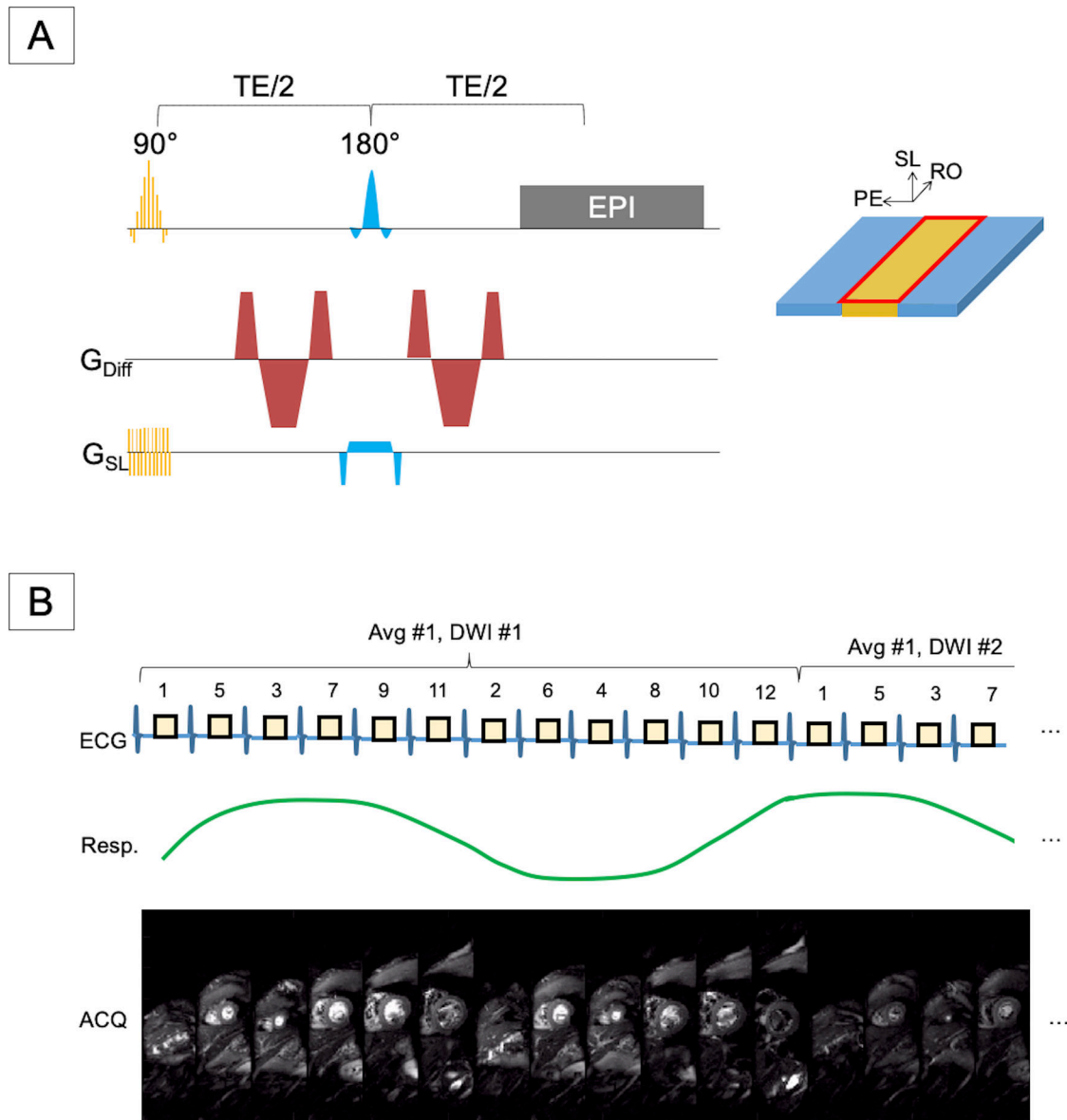


Figure 1 –.
 (A) Pulse sequence diagram of the M2 cardiac DT-MRI sequence incorporating B1 resistant M2 encoding and the 2D inner volume excitation profile of the 90-degree RF excitation pulse. (B) Single shot acquisitions are performed every heartbeat with during free-breathing using an optimized slice interleave scheme to mitigate neighboring slice crosstalk. Representative reduced FOV raw b0 diffusion-weighted images (DWIs) for all 12 slices are shown.

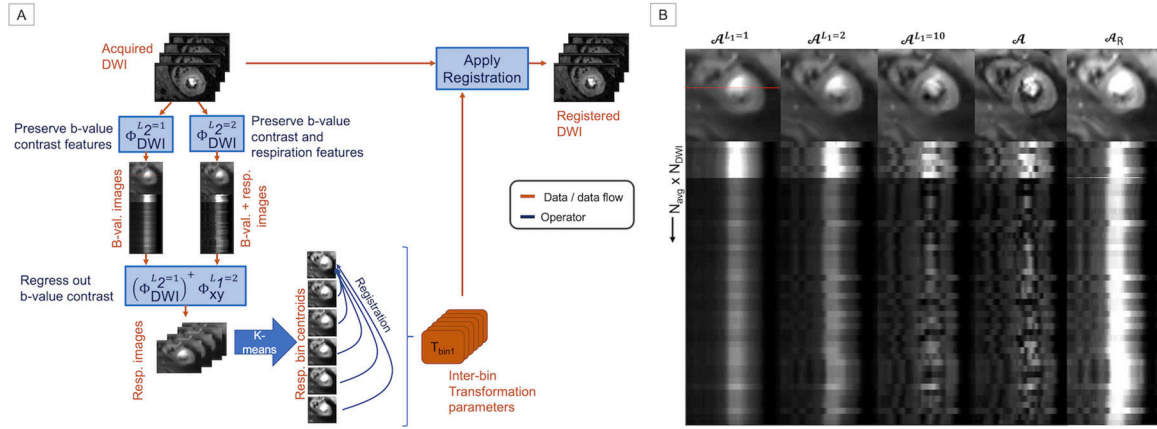


Figure 2 –. (A) MT-MOCO co-registration algorithm. Low-rank tensor decomposition is applied to acquired diffusion weighted images (DWI) to create basis functions that preserve b-value contrast features only ($\Phi_{DWI}^{L_2=1}$) and preserve both b-value contrast features plus respiratory features ($\Phi_{DWI}^{L_2=2}$). Regression of the b-value contrast is then performed to generate \mathcal{A}_R which are then binned via k-means clustering. After binning of \mathcal{A}_R into N distinct respiratory bins via k-means clustering, the centroids of each bins are co-registered, and the resulting transforms then can be applied to the original full rank DWIs according to their respective bin. Note the co-registration computational component of MT-MOCO is fixed to N number of bins regardless of the number of DWIs acquired. (B) Representative low rank tensor reconstructions with varying rank ($L_1 = 1, 20, 10,$ and full rank) of the Φ_t measurement basis matrix. Line plot through the horizontal red line of the ventricle as a function of time (vertical axis) demonstrates that $L_1 = 2$ faithfully captures the respiratory induced motion shifts in the DWIs while removing the subtle contrast differences due to changes in diffusion encoding direction. By regressing $\mathcal{A}^{L_1=1}$ reconstructed images from $\mathcal{A}^{L_1=2}$, the respiratory-only reconstructions (\mathcal{A}_R) are generated for binning and co-registration.

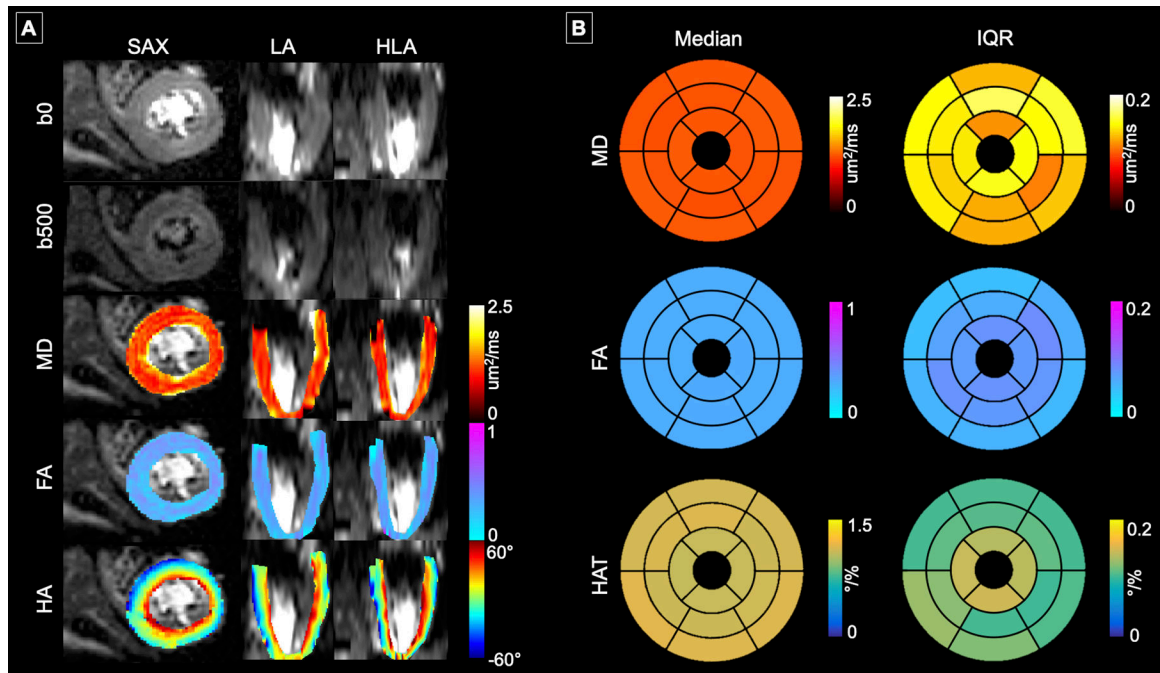


Figure 3 –.

(A) Images of the raw b0 and b500 diffusion-weighted images in the short axis, long axis, and horizontal long axis views revealing whole LV coverage. Matching MD, FA, and HA maps are shown calculated from MT-MOCO and 4 averages. MD, FA and the transmural distribution of HA all fall within the expected range of values. (B) American Heart Association (AHA) segmentation maps of the median and interquartile range (25% to 75%) of the healthy volunteers reveal consistent MD, FA, and HAT values across all segments.

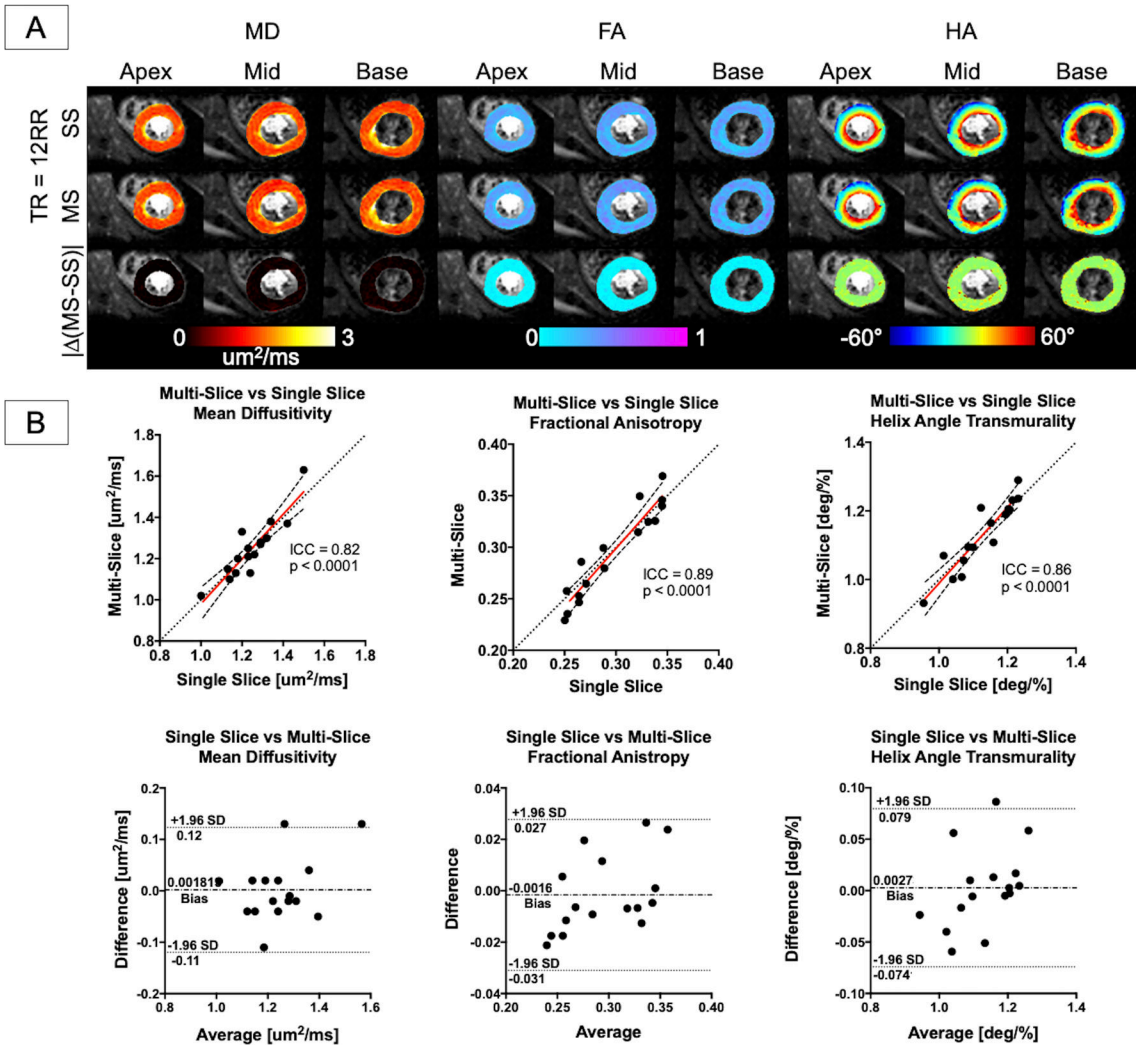


Figure 4 –. Regional comparison of the MS-12RR and SS-12RR approaches. (A) MD, FA, and HA maps at the apex, mid, and base of the LV are substantially similar with both techniques. (B) Correlation and Bland-Altman plots of global MD, FA, and HAT show a significant correlation and minimal bias between the MS-12RR (multi-slice) and SS-12RR (single-slice) techniques.

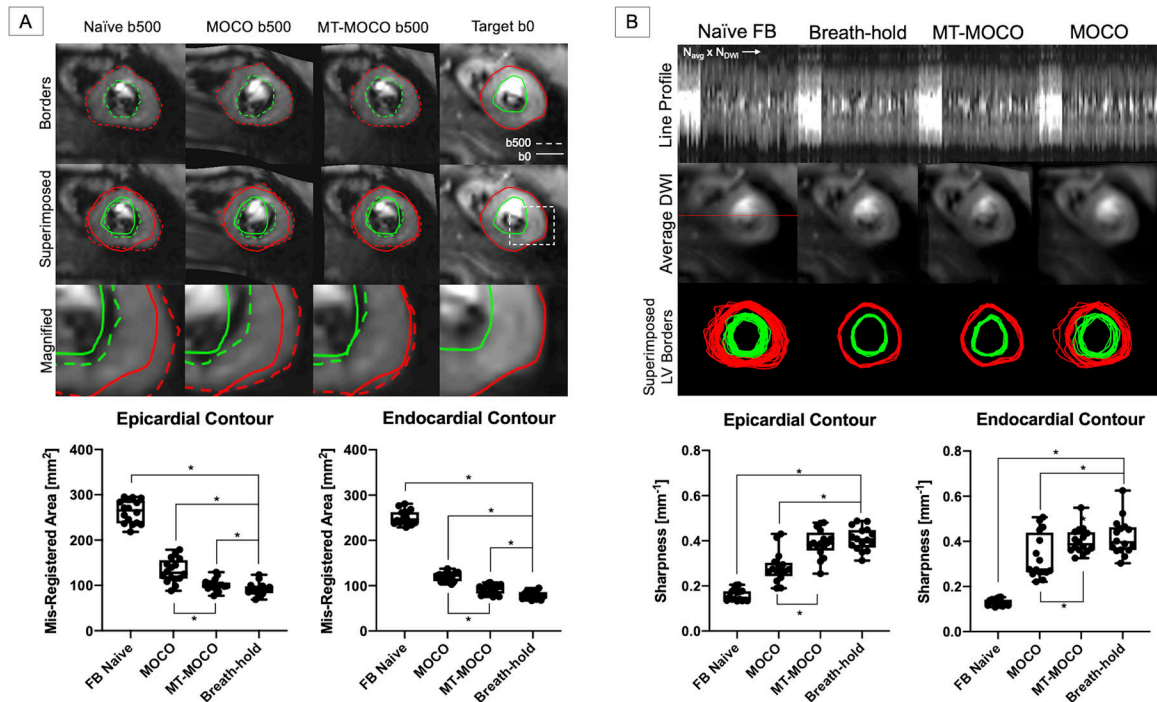


Figure 5 –.

Comparison of naïve free-breathing, conventional MOCO, and MT-MOCO reconstructions. (A) Co-registration of a b500 DWI with a target b0 image at two disparate respiratory phases using conventional MOCO and MT-MOCO. Endocardial (green) and epicardial (red) borders are depicted for naïve, conventional MOCO, and MT-MOCO b500 images (dashed lines) along with the target borders in the b0 image (solid lines). In the second row the borders derived from the b500 images (dashed lines) are superimposed on the b0 target borders (solid lines). A magnified view in the third row shows substantially more mismatch in the conventional MOCO versus MT-MOCO reconstruction. Quantification of the mis-registered area for the epicardial and endocardial borders across all subjects shows the greatest increase for the naïve and conventional MOCO reconstructions, and significantly less mis-registration area with MT-MOCO. (B) Representative line profiles through the mid-LV (dashed line), rotated and plotted along the vertical axis for all the measurements acquired over time (horizontal axis). Also shown are the averaged DWIs and LV borders superimposed on one another for all the reconstructed images. The line profiles, DWIs and LV borders show substantially less blurring with MT-MOCO vs. conventional MOCO. LV sharpness across all subjects was significantly increased with MT-MOCO vs. conventional MOCO, and was very similar to breath-hold. Both MOCO and naïve free-breathing reconstructions produced significant decreases in LV sharpness.

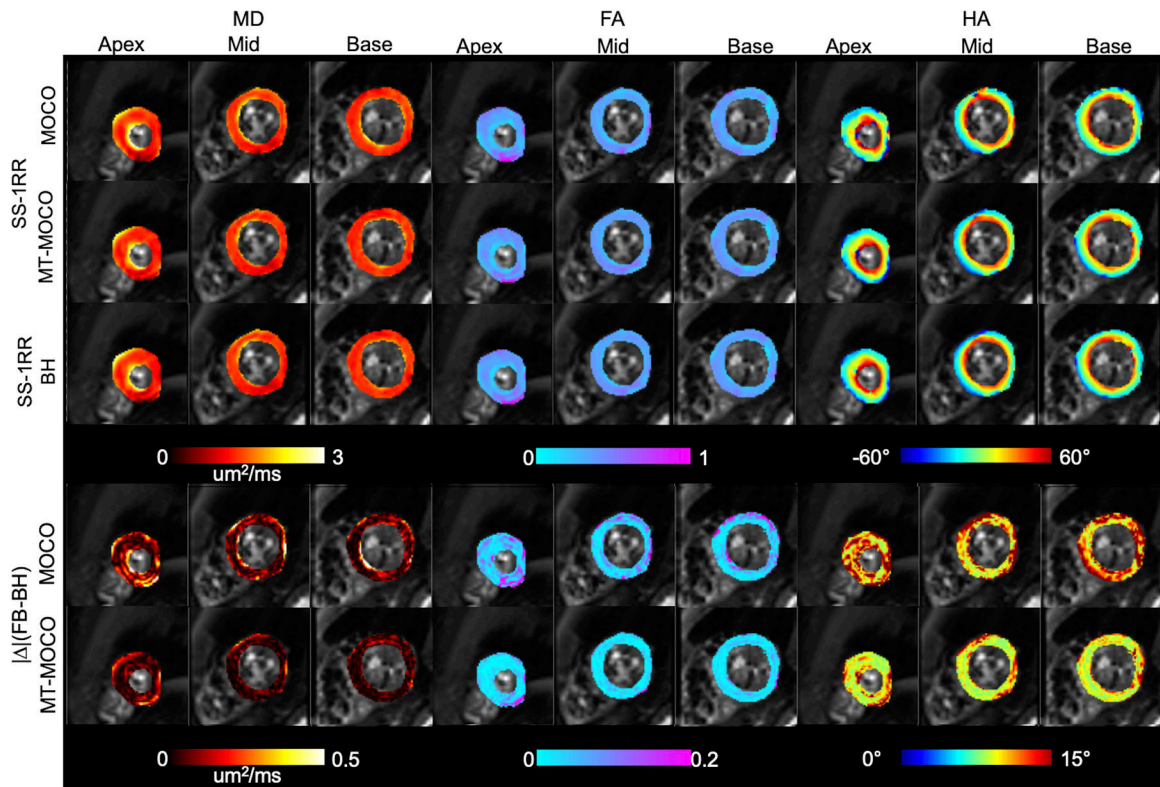


Figure 6 –.
 Comparison of SS-1RR MT-MOCO and conventional MOCO DT-MRI parameter maps. MD, FA, and HA show a high degree of similarity between the breath-hold (BH) and free-breathing (FB) approaches when MT-MOCO is performed. However, in the absence of MT-MOCO substantial differences are present between the BH and FB techniques (compare difference maps in 4th row [BH and conventional MOCO] vs. 5th row [BH and MT-MOCO]).

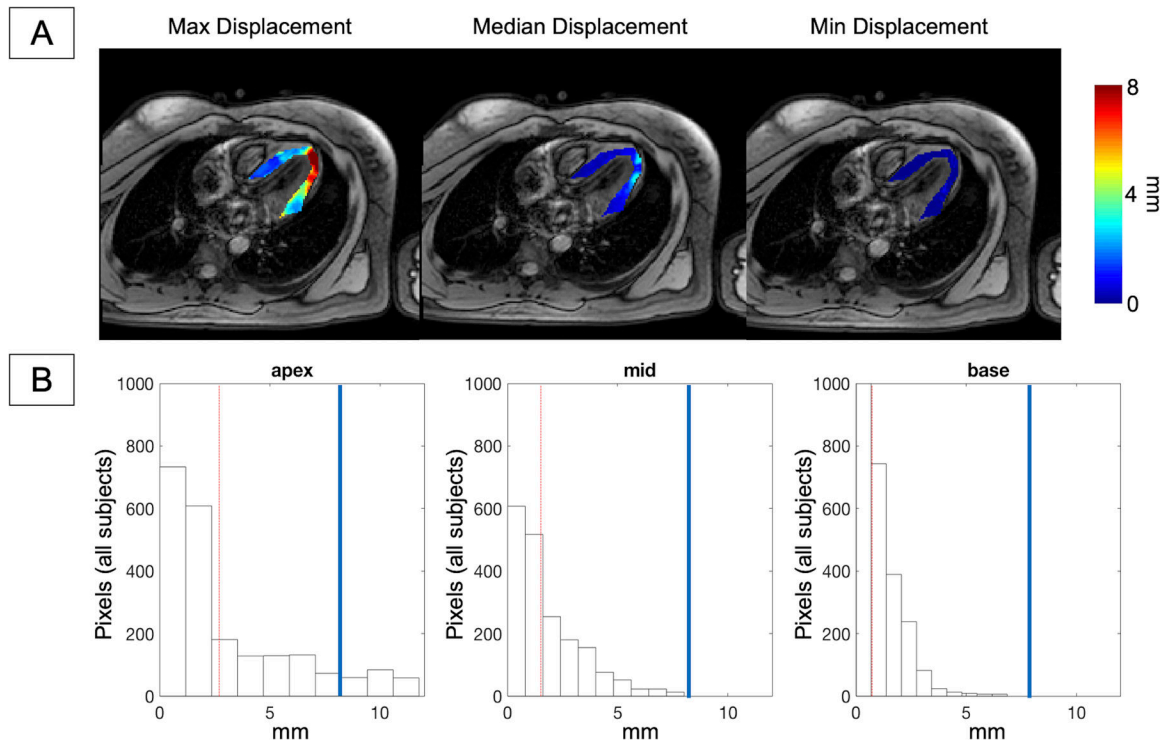


Figure 7 –.

(A) Single shot SSFP long axis images with displacement maps overlaid, showing the max, min and median values for voxel displacement over the entire respiratory cycle. (B) Through-plane displacement histograms revealed significantly more motion in the apical slices (2.7 [6.9] mm) across all subjects compared to the mid (1.5 [3.9] mm) and base (0.84 [4.2] mm), with median displacement demarked with the red dotted line. The maximum values of displacement exceed slice thickness only at the apex of the LV.

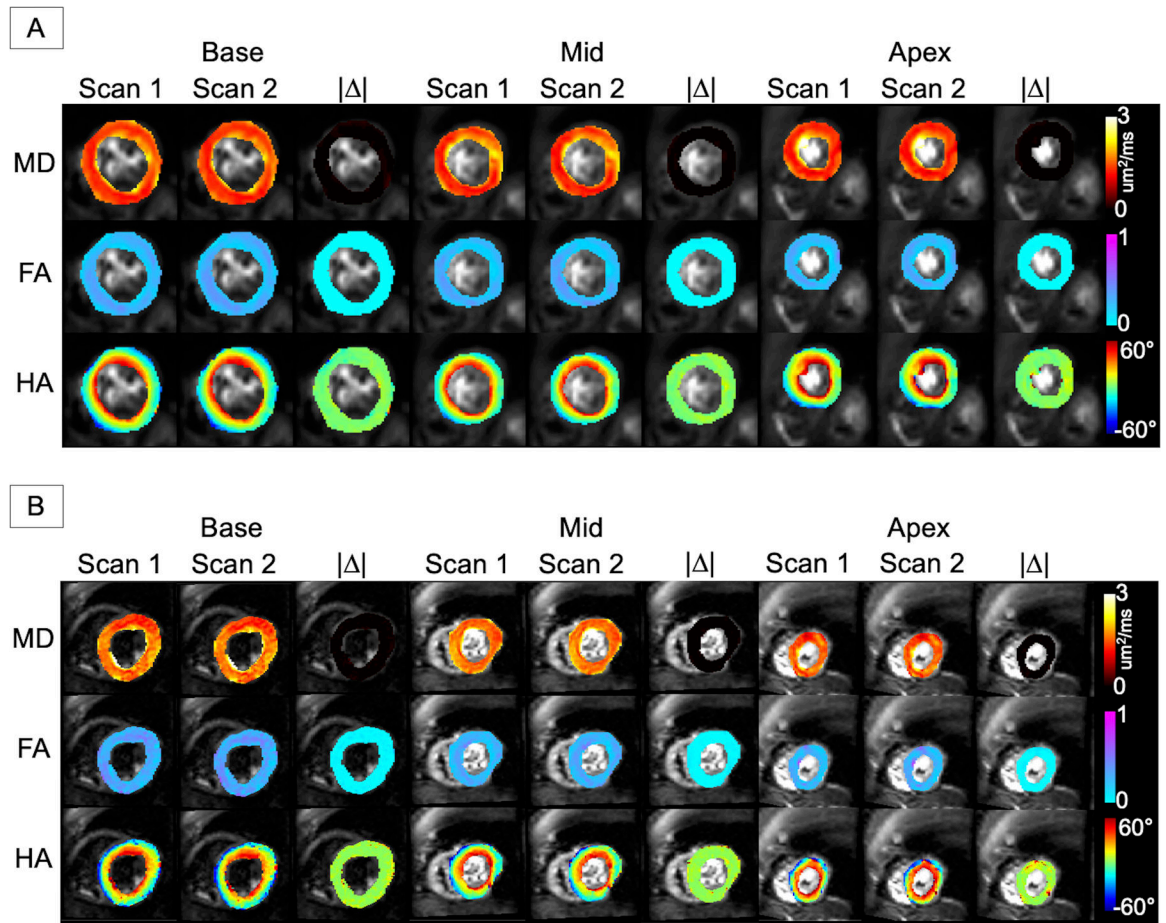


Figure 8 –. Repeatability of free-breathing MT-MOCO DT-MRI technique. (A) MD, FA, and HA maps at base, mid, and apical short axis slices acquired with the MS-12RR approach in two scans separated by at least 30 minutes. (A) normal volunteers and (B) heart failure subjects. In all cases, minimal differences were present between the two scans.

Table 1 –

Four protocols to test whole LV free-breathing M2-MT-MOCO DT-MRI

Protocol	MS-12RR	SS-12RR	SS-1RR-BH	SS-1RR
Slice Ordering	Interleaved multi-slice	Sequential single-slice	Sequential single-slice	Sequential single-slice
Respiratory Acquisition	Free Breathing	Free Breathing	Breath-hold	Free Breathing
TR	12RR	12RR	1RR	1RR
N_{DWI}	12+1b0=13	12+1b0=13	12+1b0=13	12+1b0=13
N_{AVG}	4	4	8	8
N_{slices}	12	3	3	3
Scan time (60BPM)	624 RR (10 min)	1872 RR (30 min)	312 RR (10 min with recovery)	312 RR (5 min)

Author Manuscript

Author Manuscript

Author Manuscript

Author Manuscript

Table 2 –

MD, FA, and HAT values at base, mid, and apex with the tested protocols

Protocol		MS-12RR	SS-12RR	SS-1RR		SS-1RR-BH
Reconstruction		MT-MOCO	MT-MOCO	MOCO	MT-MOCO	Breath-hold
MD ($\mu\text{m}^2/\text{ms}$)	Base	1.25 [0.11]	1.25 [0.13]	1.19 [0.29]	1.08 [0.11]	1.07 [0.18]
	Mid	1.11 [0.16]	1.06 [0.22]	1.41 [0.26] ⁺	1.28 [0.22]	1.22 [0.22]
	Apex	1.28 [0.23]	1.26 [0.20]	1.57 [0.30] ⁺	1.32 [0.32]	1.35 [0.17]
FA	Base	0.29 [0.02]	0.32 [0.05]	0.36 [0.01]	0.28 [0.04]	0.29 [0.02]
	Mid	0.24 [0.06]	0.26 [0.03]	0.38 [0.09] ⁺	0.31 [0.08]	0.26 [0.04]
	Apex	0.36 [0.04]	0.34 [0.11]	0.45 [0.14] ⁺	0.33 [0.09]	0.31 [0.09]
HAT (%)	Base	1.08 [0.08]	1.11 [0.14]	1.02 [0.14]	1.16 [0.15]	1.16 [0.10]
	Mid	1.04 [0.12]	1.10 [0.07]	0.95 [0.24]	1.11 [0.20]	1.02 [0.12]
	Apex	1.17 [0.13]	1.21 [0.17]	0.92 [0.31] ⁺	1.23 [0.20]	1.21 [0.17]

P < 0.05 for *MS-12RR vs SS-12RR; P < 0.025 for #SS-1RR MT-MOCO vs SS-1RR-BH,

⁺ SS-1RR conventional MOCO vs SS-1RR-BH.

Author Manuscript

Author Manuscript

Author Manuscript

Author Manuscript